A novel hemocompatible core@shell nanosystem for selective targeting and apoptosis induction in cancer cells

Guillermo Aragoneses-Cazorla,[a] *Juana Serrano-Lopez,*[b] *Ines Martinez-Alfonzo,*[b] *María Vallet-Regí,*[c,d] *Blanca González,*[c,d,]* *Jose L. Luque-Garcia*[a,]*

[a] Department of Analytical Chemistry, Faculty of Chemical Sciences, Complutense University of Madrid, 28040, Madrid, Spain.

[b] Experimental Hematology Lab, IIS-Fundación Jiménez Díaz, UAM, Madrid, 28040 Spain.

[c] Department of Chemistry in Pharmaceutical Sciences, Faculty of Pharmacy, Complutense University of Madrid, Instituto de Investigación Sanitaria Hospital 12 de Octubre (i+12), 28040, Madrid, Spain.

[d] Centro de Investigación Biomédica en Red de Bioingeniería, Biomateriales y Nanomedicina (CIBER-BBN), Spain.

* Corresponding authors.

E-mail addresses: jlluque@ucm.es (J.L. Luque-Garcia), blancaortiz@ucm.es (B. González)

ABSTRACT

One of the main problems with drug-based cancer treatments is the lack of selectivity, which causes them to be distributed non-specifically in the body and cells, generating undesirable side effects. In this work, a novel hybrid nanosystem for cancer cell targeting and therapeutic delivery of Ag nanoparticles has been designed. The proposed nanosystem contains a Ag core coated with a mesoporous silica shell which prevents the aggregation of Ag nanoparticles and allows the anchoring of transferrin as a targeting ligand, thus enabling the nanosystem to be selectively directed to cancer cells that overexpress transferrin receptors. The analytical and functional characterization of the nanosystem has allowed to demonstrate the selective internalization and its cytotoxic potential in cancer cells where it induces apoptosis. Additional bioanalytical experiments have enabled the identification of different transcripts and altered proteins in cells treated with the nanosystem, which has made it possible to delve deeper into the biomolecular mechanisms by which the nanosystem exerts its action. Furthermore, a hemocompatibility study indicates neither activation of monocytes nor platelet aggregation after nanosystems exposure, hence supporting a future clinical applicability of Ag@MSNs-Tf nanosystem.

Keywords: Mesoporous silica nanoparticles, silver nanoparticles, core@shell nanosystems, nanoparticles hemocompatibility, cancer treatment, active targeting, apoptosis induction, apoptosis-related proteins expression.

Electronic Supplementary Information Summary

Characterization techniques (page 2); References of TaqMan gene expression assays used for the RTqPCR analysis (Table S1, page 3); Fluorescence microscopy image of Ag@MSNs-Tf (Figure S1, page 3); TEM micrograph of Ag@MSNs, histogram of diameters from TEM and polydispersity index (Figure S2, page 4); Powder X-ray diffractogram of Ag@MSNs (Figure S3, page 5); Nitrogen adsorption measurements (Figure S4, page 6); Zeta potential and hydrodynamic size distributions of nanosystems in different media (Figure S5, page 6).

1. Introduction

Nowadays, one of the main drawbacks of cancer therapy is the non-specific distribution of the chemotherapeutic agents within the body, which leads to different issues such as significant side effects, development of multidrug resistance or metastasis, among others.[1,2] Recently, nanotechnology is playing an important role in solving this problem, by developing new nanosystems capable of being selectively targeted at tumor cells.[3] These nanosystems, on the one hand, transport chemotherapeutic agents much more effectively improving their stability, blood circulation and half-life times and, on the other hand, minimize the impact on healthy cells, thus reducing side effects.[1,4] Nanomaterials can accumulate in solid tumor tissues due to the enhanced permeability and retention effect (EPR), which contributes to a more efficient delivery of the chemotherapeutic agents to the tumor environment and constitutes the so-called passive targeting.[5,6] In addition to the passive targeting, a selective and active targeting can be achieved by incorporating to the nanosystem ligands able to recognize certain specific cellular receptors, such as the transferrin receptor (TfR), which are over-expressed in tumor cells.[7-9]

Among the different types of nanomaterials for drug delivery systems, mesoporous silica nanoparticles (MSNs) have gained great attention due to their unique properties as their tunable size, large surface areas and pore volumes, and high biocompatibility.[10-15] In addition, the high density of silanol groups displayed by MSNs allows the modification of their surface with a wide range of ligands. Thus, MSNs are ideal candidates for the design of multifunctional nanoplatforms facing cancer treatment allowing safe transport of chemotherapeutic agents and immobilization of targeting ligands to enable their selectivity towards cancer cells. Furthermore, MSNs allow the design of stimuli-responsive nanosystems[13,14] and their combination with living organisms, such as bacteria as nanoparticle carriers, improves the distribution of cytotoxic drugs within tumoral tissues.[16]

Silver nanoparticles (AgNPs) are commonly used in several biomedical applications including as anti-bacterial, anti-fungal or anti-viral agents, due to their unique physical and chemical properties. More recently, AgNPs have also been proposed as antitumoral agents due to their anti-angiogenic properties and their inhibitory effect on tumor growth.[17-20] On the one hand, AgNPs can directly induce the formation of reactive oxygen species (ROS) when they are exposed to the acidic environment of the lysosomes; on the other hand they can release Ag^+, leading to the production of ROS that induce oxidative damage to DNA and proteins, and the apoptotic cell death via mitochondrial pathways.[17,19] However, uncoated AgNPs tend to aggregate, what difficult their cellular distribution and thus, restrict their cytotoxic effects.[21] Moreover, AgNPs not only affect tumoral cells, but also healthy cells from different organs and tissues, thus potentially inducing significant side effects.[20] These two facts make it necessary to vehicle AgNPs by designing a nanosystem able to selectively deliver AgNPs to cancer cells.

In this context, different nanocomposites of AgNPs in MSNs have been previously prepared by our group such as a core@shell nanosystem (Ag@MSNs) with antimycobacterial activity against *Mtb* [22] or a nanosystem based on MSNs externally functionalized with Tf in which AgNPs were nucleated and immobilized (MSNs-Tf-AgNPs). This last nanosystem exhibits cancer cell targeting and cytotoxic effects on the cancer cells overexpressing transferrin receptors through the *"lysosome-enhanced Trojan horse effect"* mechanism.[23] Based on the promising therapeutic effect obtained in our previous study, in the present work we have designed a novel core-shell nanosystem consisting of AgNPs as core surrounded by a mesoporous silica shell whose surface has been modified by covalently anchoring transferrin as a targeting ligand (Ag@MSNs-Tf). An exhaustive analytical and functional characterization of the material has been carried out demonstrating its homogeneous and reproducible synthesis, as well as its selective internalization and cytotoxic effect in tumor cells that overexpress transferrin receptors. Furthermore, a hemocompatibility study based on circulating monocytes and platelet activation after nanosystems exposure has been performed. Likewise, the biomolecular mechanisms of action of the nanosystem have been studied in depth, giving insights on the activation of different apoptotic mechanisms by the nanosystem, as a relevant aspect and added value to the study. Reported applications of this core@shell configuration of AgNPs covered by mesoporous silica are focused on infection treatment, where the AgNPs act as antibacterial agents,[22,24-26] therefore a novel aspect of this investigation is the application of Ag@MSNs nanosystems as therapeutic against cancer.

2. Materials and methods

2.1. Reagents and equipment

Fluorescein isothiocyanate (FITC), tetraethylorthosilicate (TEOS), cetyltrimethylammonium bromide (CTAB), N-(3-dimethylaminopropyl)-N'-ethylcarbodiimide hydrochloride (EDC.HCl), 2-morpholinoethanesulfonic acid (MES) monohydrate, transferrin human (Tf), silver nitrate 99.9% and water (HPLC grade) were purchased from Sigma-Aldrich. 3-Aminopropyltriethoxysilane 97% (APTS), 3-(triethoxysilyl)propylsuccinic anhydride 94% (TESPSA) were purchased from ABCR GmbH & Co.KG. All other chemicals (formaldehyde, ethyl acetate, absolute EtOH, dry toluene, NaOH, HCl, etc.) were of the highest quality commercially available and used as received. Milli-Q water (resistivity 18.2 MΩ·cm at 25 °C) was used in all experiments.

The analytical techniques used for the characterization of the synthesized materials were as follows: thermogravimetric and differential thermal analysis (TGA and DTA), chemical microanalysis, Fourier transformed infrared (FTIR) spectroscopy, low- and high-angle powder X-ray diffraction (XRD), transmission electron microscopy (TEM), energy dispersive X-ray spectroscopy (EDS), N_2 adsorption porosimetry, electrophoretic mobility measurements to calculate the values of the zeta-potential (ζ) and dynamic light scattering (DLS). The equipment and conditions used are described in the Supporting Information.

2.2. Synthesis of Ag@MSNs

Green-emitting fluorescent Ag@MSNs were obtained following a modification of a previously published synthetic approach.[26] Under N_2 atmosphere, 5 μL of APTS (0.023 mmol) were added over a stirred solution of 2 mg of FITC (0.005 mmol) solution in 250 μL of ethanol to obtain a silylated derivative of fluorescein. The reaction mixture was stirred at room temperature for 2 h in the dark. Then, 30 μL of the resulting solution were added to a mixture of 100 μL of ethanol and 535 μL of TEOS (2.4 mmol). Separately, 50 mL of a 5.5 mM CTAB solution containing 300 μL of a 2 M NaOH solution was preheated at 80 °C for 20 min. Then, under vigorous stirring, 300 μL of a 1 M formaldehyde solution was added followed by the dropwise addition of 1 mL of a 0.1 M $AgNO_3$ solution. After 5 min, the freshly prepared TEOS and APTS-FITC mixture was added, drop by drop, and then 2 mL of ethyl acetate were added to the reaction mixture. The mixture was vigorously stirred for 2 h at 80 °C in the dark and then cooled down to room temperature. The resulting nanoparticles were collected by centrifugation at 11000 rpm for 35 min, washed three times with ethanol and finally dried.

2.3. Synthesis of Ag@MSNs-COOH

For the external surface functionalization of Ag@MSNs with carboxylic acid groups, pore surfactant containing material was employed and, therefore, approximately a quarter of the specific surface area of the free-surfactant material (669.6 m^2/g) was considered to be functionalized. Prior to surface functionalization, 350 mg of CTAB-containing Ag@MSNs (14% wt., *i.e.*, 301 mg Ag@MSNs) were dehydrated at 80 °C, under vacuum for 3 h in the dark, and subsequently re-dispersed under an inert atmosphere in 20 mL of dry toluene. The required amount of alkoxysilane derivative was calculated to achieve a maximum coverage of the external nanoparticle surface (a 100% nominal degree of functionalization) and a molar ratio of three Si-OH groups with one R-Si(OEt)$_3$ molecule was the stoichiometry used. In addition, it was presumed that the average surface concentration of Si-OH in silica materials is 4.9 OH/nm^2.[27] Therefore, a solution of 52 mg (25% exc.) of TESPSA in 10 mL of dry toluene was added to the vigorously stirred suspension of the CTAB-containing Ag@MSNs, and the mixture was heated up to 110 °C overnight in the dark. The reaction mixture was centrifuged at 11000 rpm for 35 min, and the obtained solid was exhaustively washed with toluene and ethanol. The surfactant was removed from the functionalized material by heating a well dispersed suspension of the obtained solid in an ethanol:H_2O:HCl (88:10:2) solution overnight at 80 °C. Then, the solid was washed with water and ethanol. This extraction process was repeated for 2 h and the solid was finally dried under vacuum. The Ag@MSNs-COOH$_{ext}$ material with a nominal value of -COOH groups of 9.08×10^{-4} mol/g Ag@MSN was used for the protein anchorage.

2.4. Synthesis of Ag@MSNs-Tf

Prior to the conjugation of the protein, the -COOH groups on the surface of Ag@MSNs-COOH$_{ext}$ were activated. For this activation, 81 mg (10 equiv. per nominal -COOH group) of EDC·HCl were dissolved in water and added to a vigorously stirred well-dispersed suspension of 50 mg of the Ag@MSNs-COOH$_{ext}$ material in 20 mL of Milli-Q water. The mixture was stirred at room temperature for 3 h in the dark. Then, the solid was centrifuged and rinsed with water to remove the residues of EDC. Later, activated Ag@MSNs-COOH$_{ext}$ was re-dispersed in 15 mL of a 50 mM MES monohydrate (pH 6) under gentle stirring. After that, 5 mg (1.4×10^{-3} mol per nominal -COOH group)[23] of Tf were dissolved in 4 mL of 50 mM MES monohydrate (pH 6) and added over the material suspension. The mixture was stirred overnight in the dark and centrifuged at 11000 rpm for 35 min; the solid was exhaustively washed with water and finally dried. Material was denoted as Ag@MSNs-Tf. Synthesis of materials used as controls (MSNs-Tf) were carried out as described elsewhere.[23]

2.5. Cell culture and treatment

Human hepatocellular carcinoma cell line (HepG2) was maintained in Dubelcco's modified Eagle's medium (DMEM) and mouse osteoblast-like cell line (MC3T3-E1) in alpha modified Eagle's medium (α-MEM). Both culture media were supplemented with 10% fetal bovine serum (FBS) and 1% penicillin/streptomycin at 37 °C and 5% CO_2. For performing the cell assays, cells were seeded and incubated for 24 h allowing for cell attachment before exposure to the nanosystem.

2.6. Cellular internalization

Mouse osteoblast-like cell line (MC3T3-E1) and human hepatocellular carcinoma cell line (HepG2) were seeded into 6-well plates and exposed to 50 μg/mL of Ag@MSNs and Ag@MSNs-Tf materials for 24 h. Then, cells were rinsed with phosphate buffer saline (PBS) (Fisher Scientific) and harvested using a 0.25% trypsin/EDTA solution. Cells were centrifuged at 1500 rpm for 5 min and resuspended in PBS for analysis by flow cytometry. Trypan Blue (0.4%) (Sigma-Aldrich) was added to quench the fluorescence of the Ag@MSNs adhered to the outer membrane of the cells. Then, the intensity of the green fluorescence of the positive cells was measured.

2.7. Cytotoxicity assays

For the cell viability assay, HepG2 cells were seeded on 96-well plates 24 h prior to the experiment. After cell attachment, they were exposed to 10, 15 and 25 μg/mL of MSNs-Tf and Ag@MSNs-Tf for 72 h. After this time, 20 μL of 3-(4,5-dimethyl-thiazol-2-yl)2,5-diphenyl tetrazolium bromide (MTT, 5 mg/mL) were added to each well and incubated for 4 h at 37 ºC. Then, MTT solution was removed and 100 μL of dimethyl sulfoxide (DMSO) were added to dissolve the insoluble purple formazan crystals. Then, the absorbance at 595 nm was measured using a microplate reader (TECAN).

For the cell death assay, HepG2 cells were seeded on 6-well plates and exposed to MSNs-Tf and Ag@MSNs-Tf (10 and 15 μg/mL) for 72 h. Then, cells were harvested and stained with a trypan blue solution (0.4%). The percentages of live and dead cells were obtained by counting the unstained (live) and stained (dead) cells using a Neubauer chamber.

2.8. Hemocompatibility assays

For immunophenotype changes in circulating monocytes, a small volume (100 μL) of whole peripheral blood (PB) was incubated with 50 and 100 μg/mL of Ag@MSNs or Ag@MSNs-Tf for two hours at 37 ºC. Then, monocytes activation was analyzed by fluorescence-activated cell sorter (FACS) and erythrocytes-depleted PB cells were stained for specific surface markers with phycoerythrin dye-(PE) conjugated anti-CD14 (Clone M5E2), fluorescein isothiocyanate (FITC)-conjugated anti-CD16 (Clone 3G8) and allophycocyanin (APC)-conjugated anti-CD11B. All monoclonal antibodies were purchased from BD, Pharmingen. Cell acquisition was performed by flow cytometry Canto-II (BD Biosciences) equipped with FACSDIVA™ software (BD, Biosciences) for multiparameter analysis of the data.

To determine platelet activation, citrate platelet rich plasma (PRP) was freshly isolated from healthy donors and incubated in presence of 50, 100 and 200 μg/mL of Ag@MSNs or Ag@MSNs-Tf for 20 min at 37 ºC in a platelet aggregometer TA-8V (Stago, Saint-Ouen-l'Aumône, France), following industry recommendations with minor modifications. At real time, clumps of platelets were measured by light transmission aggregometry (LTA). Epinephrine and thrombin-like peptides (TRAP) were used as soluble agonists for platelet activation.

2.9. Cell cycle analysis

Potential changes on the cell cycle pattern were evaluated on HepG2 cells treated with Ag@MSNs-Tf (10 μg/mL and 72 h). After the exposure time, cells were harvested and resuspended in 1 mL of a fixing solution containing 70% ethanol. Cells were rinsed and then incubated for 1 h at 37 °C with a 10 mg/ml RNase A solution (Invitrogen). Finally, 20 μL of a 1 mg/mL propidium iodide solution were added and the DNA content was analyzed using a FACScan flow cytometer (Becton Dickinson).

Additionally, the mRNA levels of cell cycle related genes were measured in HepG2 cells exposed to Ag@MSNs-Tf (10 μg/mL and 72 h). Total RNA was isolated using the TRIzol® reagent (Invitrogen) according to the manufacturer’s instructions. The quantity of extracted RNA was measured using a NanoDrop One (Thermo Fisher Scientific). Synthesis of cDNA with integrated removal of genomic DNA contamination was performed using a Quantitec reverse transcription kit (Qiagen) employing 1 μg of RNA. RT-qPCR analysis was carried out using TaqMan gene expression assays (Thermo Fisher Scientific) and TaqMan Fast advance master mix (Thermo Fisher Scientific) according to the manufacturer’s instructions. The references of the TaqMan gene expression assays used are listed in Table S1 in Supporting Material. All reactions were performed in a final volume of 10 μL. The reaction protocol was 2 min at 50 °C, 10 min at 95 °C for activating the polymerase and 40 cycles of 15 s at 95 °C and 1 min at 60 °C. Relative expression of genes was normalized using GADPH as the endogenous control. Gene expression in each sample was calculated as $2^{-\Delta\Delta Ct}$.

2.10. *Apoptosis proteins array*

Simultaneous evaluation of the expression of key apoptosis-related proteins was carried out using the Proteome^{TM} Profiler Human Apoptosis Array Kit (R&D systems). After exposure to Ag@MSNs-Tf, cells were lysed in buffer containing protease inhibitors (Thermofisher) and the total protein concentration was determined by means of the Bradford assay. Then, lysates containing 300 µg of protein were processed following the manufacturer´s instructions. Images were obtained with a Fujifilm LAS-3000 Imager after an exposure time of 5 min and pixel density of each signal was measured using the Image J program (NIH).

2.11. *Statistical analyses*

Unless otherwise stated, all experiments were performed in quintuplicate (n = 5). Data were analyzed by ANOVA followed by Bonferroni's multiple-comparison test in GraphPad Prism version 6.0.

3. Results and Discussion

3.1. *Synthesis and characterization of the nanomaterial*

The synthetic approach for obtaining the novel hybrid nanosystem consisting on core@shell nanoparticles functionalized with Tf as a vectorization ligand (Ag@MSNs-Tf) is shown in Figure 1. Ag cores were formed in a first step using $AgNO_3$ as a source of Ag^+, which was chemically reduced in a basic solution containing CTAB as stabilizing agent. This surfactant also acts as template in the subsequent step where the AgNPs are the nucleus or seeds for the polymerization of the alcoxysilane precursor TEOS that leads to the formation of the mesoporous silica shell through hydrolysis and condensation (Figure 1A). A fluorescent dye was covalently linked to the silica network through a co-condensation reaction during the silica shell formation to make the nanosystem traceable in the *in vitro* cell studies (See Figure S1). To get this, fluorescein isothiocyanate was reacted with 3-aminopropyltriethoxysilane in a previous reaction and the in-situ-generated intermediate was mixed with the TEOS (TEOS/APTS-FITC).[28] Ethyl acetate was added in this last step to control the morphology of the final nanoparticles during the sol-gel reactions.[26] Then, the protein Tf was covalently anchored in the external surface of Ag@MSN (Figure 1B) following a standard bioconjugation reaction of carbodiimide-mediated coupling between carboxylic acids and amines in aqueous media.[23,29-31]

For that, carboxylic acid groups were firstly introduced in the surface of the surfactant containing Ag@MSN material through a post-functionalization method under water free conditions using TESPSA. The carboxylic acid groups are afforded because the hydrolysis and ring opening of the succinic anhydride group is produced during the surfactant extraction.[23,32] Then, taking advance of the carbodiimide chemistry, the carboxylic acid groups were activated to covalently bond the protein through the condensation of some of the $–NH_2$ of amino acids of Tf with the –COOH, which leads to the formation of amide bonds.[23]

Ag@MSN material was first characterized by TEM confirming the presence of a single silver core inside the mesoporous silica nanoparticles in a typical core@shell structure. The obtained Ag@MSNs were quite homogeneous regarding morphology, with average diameters of *ca.* 55 nm and 15 nm for the Ag@MSNs and the Ag core, respectively (Figure 2A and 2B). The dispersity value or polydispersity index calculated for Ag@MSNs sample from size measurements of nanoparticles in the TEM images has a value of 0.138 (see Figure S2 in ESI). Therefore, it can be considered that the size distribution of Ag@MSNs nanosystem, with a value lower than 0.2 and close to 0.1, tends to be highly monodisperse because a sample is considered monodisperse when the PdI value is less than 0.1.[33,34]

The silica shell exhibits wormhole-like mesopores radially arranged from the center. The atomic percentages for silver and silicon of Ag@MSNs were estimated by EDS analysis (see inset in Figure 2A), showing a composition of 5% Ag and 95% Si. High-angle XRD measurements verified that the cores were exclusively formed by metallic Ag, displaying the characteristic diffraction pattern of this element (Figure S3 in ESI).

N_2 sorption measurements were performed to analyse the textural properties of these core@shell nanoparticles (Figure S4 in ESI). N_2 adsorption-desorption analyses of the Ag@MSN material exhibit the characteristic type IV BET isotherms confirming their channel-like mesoporous structure. The isotherm shows a more pronounced growth in the increase of the amount of adsorbed nitrogen in the range of P/P_0 0.3 to 0.4, ascribed to the capillary condensation in mesopores. The surfactant free material possesses a high surface area of 669.6 m^2/g and a large pore volume of 0.53 cm^3/g after subtraction of the interparticle porosity. An average pore diameter of 2.5 nm was calculated from the maximum of the pore size distribution.

The functionalization stages of the Ag@MSNs surface were monitored by the determination of the organic content of the materials by TGA and chemical analysis (Table 1). The results confirmed the expected increase of the organic content and %C after the functionalization of the bare fluorescent Ag@MSNs with the alkoxysilane to introduce the –COOH groups in the first step and with transferrin (Tf) in the last one. Furthermore, the increase in the N and S content after protein incorporation can be ascribed to amino acids from the transferrin.

In addition, the successive incorporation of the new –COOH and Tf functionalities in the Ag@MSNs nanosystem has been followed by means of FTIR spectroscopy (see Figure 3). For the first functionalization step it is observed a change in the 1900-1300 cm^{-1} range from a clean spectrum for Ag@MSNs to the appearance of a new band at 1716 cm^{-1} due to the stretching mode ν(C=O) of carboxylic acid groups in Ag@MSNs-COOH. Then, in the same region in the FTIR spectrum of Ag@MSNs-Tf, the presence of two signals at 1647 and 1541 cm^{-1}, which are characteristic of the C=O stretching vibration (ν(C=O), amide I) and N-H bending vibration (δ(N-H), amide II), respectively, is clearly observed. The amide group is present in the transferrin because it is the peptide bond linking the amino acids in the primary structure of proteins. The appearance of the broad band due to the NH stretching mode of the amide group around 3338 cm^{-1} is also clear. These facts reflect the presence of transferrin in the final Ag@MSNs-Tf nanosystem. The presence of a large number of amide bonds somehow masks the identification of the new amide bonds formed through carbodiimide chemistry to bind transferrin to the carboxylic acids on the surface of the Ag@MSNs-COOH nanosystem. However, the displacement or transformation in a shoulder of the C=O stretching band due to the partial consumption of the carboxylic acids of the material Ag@MSNs-COOH would support the formation of new amide bonds in the Ag@MSNs-Tf nanosystem. Bands due to ν(C-H) from CH_2 groups can be observed in the three spectra. They correspond to ethoxy groups from incomplete hydrolysis and condensation during the sol-gel reactions for the silica shell formation in Ag@MSNs material, to the methylene chain of the TESPSA alkoxysilane incorporated in the first functionalization step, and the methylene groups in transferrin incorporated in the last one. Bands due to silica are indicated in Figure 3, together with their assignations to the vibrational mode and structural unit from the inorganic shell of the nanosystems.

Additionally, zeta-potential (ζ-potential) measurements were performed to follow the functionalization process (Table 2 and Figure S5.A). Bare Ag@MSNs material displayed negative charge of *ca.* −14 mV due to the silica shell possessing silanol groups that dissociate in water following an acid-base equilibrium ($R\text{-}Si\text{-}OH + H_2O \rightleftharpoons R\text{-}SiO^- + H_3O^+$). After functionalization with TESPSA the ζ-potential exhibits a more negative value due to the -COO^- groups from the new carboxylic acid functionalities ($R\text{-}COOH + H_2O \rightleftharpoons R\text{-}COO^- + H_3O^+$). The ζ-potential value shifts again towards a less negative value after the covalent introduction of the Tf onto Ag@MSNs-$COOH_{ext}$ due to the consumption of a small proportion of –COOH groups. The hydrodynamic particle diameter (D_H) of the materials was measured by DLS (Table 2 and Figure S5.B). All the materials displayed monomodal and narrow hydrodynamic size distributions comprised between 30 and 110 nm, with hydrodynamic sizes that are in agreement with the ζ-potential values after functionalization. For the bare Ag@MSNs the maximum of the size distribution is found around 68 nm, which decreases to *ca.* 59 nm when the functionalization with TESPSA takes place. This fact is in accordance with the decrease of the ζ-potential which causes higher electrostatic repulsion and reduces the number and size of nanoparticle aggregates. When the Tf is attached to the external surface the maximum of the hydrodynamic size increases a smaller amount, to *ca.* 79 nm, due to two possible causes. On one hand, the less negative value of −20 mV, although still in the zone of colloidal stability, shifts the maximum of the hydrodynamic size distribution. Furthermore, the presence of the protein which is a macromolecule on the surface of the nanoparticles makes the hydrodynamic size to increase due to apparent size of the nanoparticle bigger than the inorganic core@shell nanosystem itself. Accordingly to the ζ-potential and hydrodynamic size results, Ag@MSN as well as the functionalized materials exhibit excellent dispersion and colloidal stability in water media.

In addition, the stability of Ag@MSNs-Tf in relevant media for bioanalytical assays has been investigated. Hydrodynamic diameters of Ag@MSNs-Tf measured by DLS in PBS and cell culture media also presented monomodal and narrow distributions centered at *ca.* 290 and *ca.* 68 nm, respectively (see Figure S5 in ESI). Although in PBS media the formation of larger aggregates can be detected, the material also exhibit excellent dispersion and colloidal stability in PBS and cell culture media.

3.2. Evaluation of the selective internalization of Ag@MSNs-Tf

After confirming the homogeneity and reproducibility of the synthesis, as well as the successful incorporation of Tf, the selective internalization of the Ag@MSNs-Tf material was evaluated using two cells lines, HepG2 and MC3T3-E1 cells, which show a clear difference in transferrin receptor (TfR) expression levels.[35,36] Cells were exposed to 50 μg/mL of either the bare (Ag@MSNs) and the protein decorated (Ag@MSNs-Tf) material during 24 h. Flow cytometry was used to evaluate the degree of internalization by quantifying the intensity of the fluorescence of positive cells (Fig. 4). Functionalization with Tf significantly enhanced the internalization of the material in HepG2 cells as compared with the bare material (Fig. 4). Additionally, uptake of Ag@MSNs-Tf in MC3T3-E1 cells (with low TfR expression level) was clearly lower as compared to that in HepG2 cells (with high TfR expression level). In

MC3T3-E1 cells there were no significant differences in the degree of internalization between the bare or the Tf decorated material (Fig. 4). These results confirmed the TfR mediated cellular uptake and demonstrate the selective internalization of Ag@MSNs-Tf towards cancer cells overexpressing TfR.[23]

3.3. Cytotoxicity of Ag@MSNs-Tf

Once the selectivity of the Ag@MSNs-Tf material towards cells overexpressing TfR was proved, the cytotoxic effects exerted by this material were assessed. To this end, cell viability (Fig. 5A) and cell death (Fig. 5B) assays were carried out by exposing HepG2 cells to different concentrations of Ag@MSNs-Tf and MSNs-Tf (as control) for 72 h. The effect over the cellular viability was evaluated by means of the MTT assay, which measures the reducing potential of the cells. While healthy cells are able to reduce the MTT to formazan (a purple colored compound), non-viable cells are unable to do so. Therefore, cell viability can be determined by measuring the absorbance of the MTT-treated cells at 595 nm. As shown in Fig. 5A, the viability of HepG2 cells was hardly compromised after treatment with MSNs-Tf and remained constant regardless of the concentration, showing the biocompatibility of the MSNs-Tf material. On the other hand, exposure to Ag@MSNs-Tf significantly reduced the cellular viability of the cells in a concentration-dependent manner, reaching a 40% decrease after exposure to 10 μg/mL of Ag@MSNs-Tf during 72 h, thus demonstrating that the cytotoxic effect exerted by the Ag@MSNs-Tf material can be exclusively attributed to the Ag core. Additionally, a trypan blue-based assay was performed in order to evaluate the potential of the nanosystem to induce cell death. This dye can only penetrate and stain cells whose nuclear membrane is compromised, which means that they are undergoing cellular death. The results showed that the percentage of dead cells was significantly higher in cells exposed to Ag@MSNs-Tf as compared to those exposed to MSNs-Tf. Moreover, the percentage of dead cells increased at higher concentrations of Ag@MSNs-Tf (Fig. 5B). These results are also in well agreement with the higher decrease in cellular viability observed in cells exposed to Ag@MSNs-Tf as compared to cells exposed to MSNs-Tf (Fig. 5A).

3.4. Hemocompatibility of Ag@MSNs and Ag@MSNs-Tf

Blood is the main contact for nanoparticles administered intravenously and via other routes, to reach different target tissues throughout the body.[37,38] Nanoparticles interactions with blood elements is one of the principal concerns for its approval by medical agencies. Hence, to determine the effects of Ag@MSNs and Ag@MSNs-Tf on monocytes we developed an assay to measure several markers associated with monocytes activation from whole peripheral blood of healthy donors (Figure 6A-B). A marker whose expression increases when the activation of the monocyte occurs (CD16) and another marker whose expression decreases (CD11B) were selected. After two hours being in contact, we observed an increase of mean fluorescent intensify (MFI) of CD16 for Ag@MSNs-Tf at the higher dose tested (Figure 6A) without significance. No changes were detected for CD11B (Figure 6B). Therefore, at doses less than 100 μg/mL these nanosystems do not produce monocyte activation.

On the other hand, platelet is a key component of coagulation. Once platelets become activated suffer conformational changes allowing surface integrins to build a platelet plug.[39] To determine platelet aggregation, we first isolated citrate platelet rich plasma. Then, real time measurements of platelet sedimentation were quantified after interacting with the nanosystems (Figure 6C-D). We failed to detect a significant formation of platelet aggregation after either Ag@MSNs or Ag@MSNs-Tf insult, being in all samples analyzed less than 5% (Figure 6D).

3.5. Evaluation of the action mechanisms of the nanosystem

In a second set of experiments, and with the aim of exploring in depth the biomolecular mechanisms of action of the synthesized nanosystem, its ability to induce alterations in the cell cycle and/or to induce apoptosis in cancer cells was evaluated.

3.5.1. Effect on cell cycle regulation and progression

In order to evaluate whether the designed nanosystem Ag@MSNs-Tf might be inducing cell cycle arrest or promoting the apoptotic pathways, a flow cytometry-based cell cycle assay followed by an RT-qPCR analysis of different genes involved in cell cycle control and progression (Table S1 in ESI) were carried out in the first place. As shown in Figure 7A, after exposure to Ag@MSNs-Tf there were not significant changes in the cellular population of neither Sub G0, G0/G1 nor S-G2/M phases as compared to control cells, which indicates that Ag@MSNs-Tf does not arrest the cell cycle. Nevertheless, mRNA expression levels from most of the evaluated transcripts were significantly altered in cells exposed to Ag@MSNs-Tf in comparison to control cells (Figure 7B). In this sense, the expression levels of TP53 and C-MYC transcripts were overexpressed after exposure to Ag@MSNs-Tf. As for the G1/S transition regulated by the association between cyclin E (CCNE1) and CDK2, while the mRNA level of CDK2 was found downregulated, cyclin E showed an upregulation. CDK2 is also implied in the S/G2 checkpoint alongside cyclin A2 (CCNA2), whose mRNA expression level was also inhibited in cells exposed to the nanosystem. Cyclin B (CCNB1) and CDK1, which are involved in the G2/M checkpoint, were found downregulated in HepG2 cells exposed to Ag@MSNs-Tf, suggesting that exposure to the proposed nanosystem might induce cell cycle arrest in S-G2/M phase, which beforehand could seem contradictory.[40-42]

3.5.2. Apoptosis-related proteins expression

Since the previous results showed that the nanosystem does not arrest the cell cycle and because the cell cycle related transcripts that are altered could also be affected due to the fact that the nanosystem is inducing apoptosis, the expression profile of different apoptosis-related proteins were analyzed (Figure 8A-C). In HepG2 cells exposed to Ag@MSNs-Tf almost all proteins evaluated in the array were found deregulated upon exposure. Out of the 35 proteins, only 3 of them, Pro-Caspase-3, Catalase and PON2, were not differentially expressed between control and treated samples. In order to facilitate the understanding of the mechanisms related to the expression of the evaluated proteins, the proteins were grouped in three categories according to the interactions or the processes in which they are involved.

Cell cycle-related apoptosis mechanisms. The first category comprises proteins whose expression is directly involved in the regulation of the cell cycle and are related with the induction of apoptosis (Fig. 8A and Fig. 9A). Of all the proteins found to be deregulated, the overexpression of the p53 protein, including 3 variants that consider phosphorylation in S392, S46 and S15, seemed especially relevant. p53 is a tumor suppressor which appeared inactivated in half of the human cancers, including liver cancer;[43,44] thus, the fact that exposure to Ag@MSNs-Tf induces overexpression of this protein, whose transcript was also confirmed to be highly upregulated by RT-qPCR, confers a promising anti-tumoral potential to the designed nanosystem. Furthermore, p53 has been shown to induce cell cycle arrest or apoptosis depending on its expression level; meanwhile low levels of p53 only produce cell cycle arrest, high levels of this tumor suppressor lead to cellular apoptosis through the activation of the pro-apoptotic Bcl-2 family member Bax.[45] The overexpression of Bax, together with that of cyclin E, observed upregulated by RT-qPCR, is closely related to the induction of apoptosis after cellular stress.[46,47] These facts are in agreement with the results discussed above in which it was shown that the cell cycle is not arrested after exposure to Ag@MSNs-Tf, but apoptosis is induced. Interestingly, it has also been reported that cells overexpressing cyclin E are more sensitive to Fas, TRAIL and TNF-α mediated apoptosis. Proteins Fas and TRAIL (TNFR1, DR4 and DR5) were found overexpressed after exposure to Ag@MSNs-Tf, and the association among Fas, DR4 and DR5, along with FADD (also found overexpressed) constitutes the complex DISC which triggers the cellular apoptosis via caspase-8 activation.[47-50] Activation of caspase-8 implies upregulation of the cleaved caspase-3, which is necessary for DNA fragmentation during apoptosis. This protein was also found overexpressed after treatment with the nanosystem, which is particularly relevant considering that its upregulation has been reported to be essential for inducing apoptosis after treatment with several chemotherapeutic drugs.[51,52] In addition, the mRNA level of the oncogene c-Myc was found upregulated in the RT-qPCR analysis; its overexpression can also be related to the activation of cellular apoptosis through a wide variety of pathways, in which proteins from the Bcl-2 family are also involved.[53,54] Additional cell cycle-related transcripts were found inhibited in cells exposed to Ag@MSNs-Tf. Such is the case of CDK2, whose inhibition is often related to DNA damage and it could induce apoptosis by preventing the transcription factor FOXO1 from being phosphorylated, thus enabling the upregulation of different cell death genes, like the one that encodes Fas.[55] Moreover, the inhibition of the cyclin A/CDK2 complex produces an increase on E2F level, which lastly induce cellular apoptosis.[56] Finally, the downregulation of the cyclin B1/CDK1 complex may enhance the Fas-mediated activation of caspase-8 and, therefore, the cellular apoptosis.[57] It should be noted that although the mRNA level of the cell cycle inhibitor CDKN1A (p21) was not found significantly altered in cells exposed to Ag@MSNs-Tf, the expression of the p21 protein was found significantly overexpressed in treated cells, which in principal could be contradictory. Nevertheless, it is known that c-Myc can transcriptionally repress p21 so that the overexpression of c-Myc could explain the CDKN1A transcript level.[58] In addition, although p21 generally plays an anti-apoptotic role through the activation of different anti-apoptotic factors, it has also been reported that it can exert a pro-apoptotic role since p21 could be cleaved by caspase-3, thus enhancing the cellular apoptosis after DNA damage.[58,59] Moreover, p21 can translocate to the nucleus to participate in DNA repairing processes, thus avoiding its degradation in the cytosol, what could explain the higher expression of p21 observed at the protein level.[59] Another cell-cycle inhibitor which belongs to the same family as p21 is the p27/Kip1 protein; this protein was also found upregulated, which can be considered as another indication that apoptosis is being induced by the designed nanosystems.[60]

Pro-apoptotic mechanisms. Besides the proteins directly related to the cell cycle related transcripts that were evaluated by RT-qPCR, the expression of additional pro- and anti-apoptotic proteins was also assessed (Fig. 8B). The Bcl-2 family of proteins is tightly involved in the regulation of apoptosis since it is composed by pro-apoptotic proteins such as

Bad or Bax, and anti-apoptotic proteins that include Bcl-2 and Bcl-x.[47,61] Regarding the pro-apoptotic members of this family, apart from Bax, whose function has been described above, the upregulation of Bad can induce apoptosis through the mitochondrial release of cytochrome c, SMAC/Diablo and AIF (Fig. 9B).[62,63] The release of cytochrome c from the mitochondria produces the assembly of a complex called "apoptosome" which finally results in the activation of caspase-9.[64] In addition, the overexpression of the pro-apoptotic protein SMAC/Diablo, as it was found in cells exposed to the nanosystem, has been demonstrated to contribute to induce apoptotic cell death since the interaction of this protein with the inhibitor of apoptosis protein (IAP) member XIAP in the presence of a pro-apoptotic stimuli, triggers the release of caspases-3 and -9.[65] This assertion is supported by the fact that the HTRA2/Omi protein was also found overexpressed. This protein induces activation of SMAC/Diablo and its release to the cytosol contributes to apoptosis via caspase-dependent and -independent pathways.[66]

Cellular defense mechanisms. In order to avoid cellular death, cells undergoing pro-apoptotic mechanisms or cellular stress, activate different defense pathways (Fig. 9C) in which the expression of different anti-apoptotic and defense proteins is involved (Fig. 8C). Two anti-apoptotic members of the Bcl-2 family of proteins, Bcl-2 and Bcl-x, were found overexpressed, what initially could be considered a contradiction in terms of the ability of the nanosystem to induce apoptosis. Nevertheless, these proteins usually bind to Bax in order to inhibit its action and, consequently, they can be upregulated to counterbalance the effect of the enhanced expression of their anti-apoptotic binding partner as a defense cellular mechanism.[61]

It is also important to consider that different pro-apoptotic members of the Bcl-2 family have been previously reported to be overexpressed under stress conditions, as in the case of hypoxia induced by reactive oxygen species (ROS) generated after exposure to AgNPs.[67] Under these conditions, cells can stabilize HIF-1α as an adaptative response. Such protein also plays a role in the modulation of apoptosis; its upregulation disrupt the p53-Mdm2 complex, inducing activation of p53 and thus, apoptosis.[67,68] In addition, the expression of HIF-1α directly regulates the IAP member named survivin. As a result, upregulation of HIF-1α should lead to the overexpression of survivin, as it has been observed in cells exposed to Ag@MSNs-Tf.[69] The expression levels of other IAP family members such as cIAP-1, cIAP-2, XIAP and livin were also assessed. It has been reported that under the described hypoxic conditions cIAP-2 protein can be overexpressed, as it has been seen in the results.[67]

Interestingly, the overexpression of these IAP members is usually considered a response to the treatment of cells with chemotherapeutic agents.[70-72] The expression levels of cIAP-1 and cIAP-2 are usually increased due to survival signals such as the epidermal growth factor (EGF); and what is more, the expression level of cIAP-1 is maintained in the presence of a pro-apoptotic stimuli called transforming growth factor-β (TGF-β). The presence of both factors allows the cleavage of cIAP-1 by different caspases and consequently, under these conditions, cIAP-1 can be transformed into a pro-apoptotic protein.[73] Although XIAP has an anti-apoptotic activity as inhibitor of different caspases, it has also been suggested to be necessary for increasing the TGF-β signaling.[71,73] In addition, the expression of different proteins involved in cellular defense mechanisms was also analyzed in cells exposed to Ag@MSNs-Tf. Such is the case of HSP27, HSP60 and HSP70, three members of the heat shock protein (HSP) family whose overexpression is usually observed under oxidative stress conditions. These proteins act lowering the intracellular ROS levels to protect cells from undergoing apoptosis,[74-76] so it is not surprising that they appeared upregulated in cells treated with the nanosystem. Similarly, the overexpression of the heme oxygenase (HO) proteins (HO-1 and HO-2) that has been found is also known to play a protective role against oxidative stress and other stress situations.[77,78] Finally, overexpression of proteins involved in other mechanisms related to the cellular response to DNA damage or to cell survival has also been found. Such is the case of the Rad17 protein, upregulated in cells treated with Ag@MSNs-Tf, which has been reported to be activated after DNA damage through its phosphorylation by ATR.[79,80] Moreover, phosphorylated-Rad17 interacts with claspin, also found upregulated, by promoting its recruitment.[79] Hence, the overexpression of phosphor-Rad17 contributes to the upregulation of claspin, which phosphorylates Chk1 promoting the G2/M progression after DNA damage.[81,82] In the same way, clusterin was also found upregulated in cells exposed to the designed nanosystem. Its overexpression has been associated to apoptotic events since its main function is enhancing cell survival under stress situations. Especially interesting is the fact that this protein has also been found upregulated in other studies in response to treatments with different chemotherapeutic agents.[83,84]

To sum up, the proposed nanosystem is able to induce apoptosis through the interaction of different cell cycle related components with membrane apoptotic receptors, and through the expression of pro-apoptotic proteins, triggering in both situations the activation of the caspase cascade. Moreover, the expression of the apoptotic proteins themselves and the generation of ROS associated to the action of AgNPs, induce the direct or indirect activation of different defense proteins to counterbalance the action of the ongoing apoptotic pathways.

4. Conclusion

A novel hybrid nanosystem consisting of core-shell Ag@MSNs externally modified with Tf as targeting ligand has been prepared aimed at cancer treatment. The physico-chemical characterization showed that well dispersed and homogeneous nanoparticles of *ca.* 55 nm containing 15 nm Ag cores were obtained via a highly reproducible synthetic strategy.

The functional characterization through *in vitro* assays confirmed the selective internalization of the nanosystem in cancer cells overexpressing TfR and the decrease in the viability of treated cells in a concentration dependent manner, inducing a significant percentage of cell death. Moreover, treatment with the nanosystem altered different cell cycle related transcripts such as TP53, C-MYC, CDK1, CDK2, CCNA2, CCNE1 and CCNB1. Additionally, several apoptosis-related proteins were deregulated under the action of the Ag@MSNs-Tf. Both sets of results demonstrate the activation of different apoptotic mechanisms in cells treated with the proposed nanosystem. The results have demonstrated the promising potential of the synthesized nanosystem to selectively transport AgNPs, which act as cytotoxic agents, to cancer cells. The hemocompatibility study based on circulating monocytes and platelet activation indicated that nor activation of the monocytes neither platelet aggregation was produced after nanosystems exposure at doses higher than the needed to exert their cytotoxic effect in cancer cells, supporting the future clinical applicability of Ag@MSNs-Tf nanosystem.

Overall, this Ag@MSNs-Tf nanosystem represent a platform that prevents the aggregation of Ag nanoparticles and shows selective internalization and cytotoxic capacity through the activation of different apoptotic mechanisms of cancer cells. Future studies will also explore the functionalization with other targeting moieties for overexpressed receptors in specific cancer situations, as well as the loading of the mesopores with anticancer drugs looking for a synergistic effect with the cytotoxic effect of silver in cancer cells. Moreover, further efforts are being carried out to evaluate the suitability of the proposed nanosystem in clinical applications for cancer treatment.

Declaration of Competing Interests

The authors declare that they have not known competing financial interests or personal relationships that could have appeared to influence the work reported in this paper.

Acknowledgements

This work was supported by Ministerio de Ciencia e Innovación (MINECO) grants: CTQ2017-85673-R (JLL-G) and MAT2016-75611-R (BG), and the European Research Council ERC-2015-AdG (VERDI) Proposal No. 694160 (MV-R). CIBER is a public research consortium created by ISCIII whose actions are co-funded by the European Regional Development Fund. GA-C thanks the Ministerio de Ciencia, Innovación y Universidades for a pre-doctoral fellowship (FPU18/01176).

References

[1] C.-Y. Zhao, R. Cheng, Z. Yang and Z.-M. Tian, Nanotechnology for cancer therapy based on chemotherapy, *Molecules*, 2018, **23**, 826-855.

[2] B.N. Ho, C. M. Pfeffer and A.T.K. Singh, Update on nanotechnology-based drug delivery systems in cancer treatment, *Anticancer Res.*, 2017, **37**, 5975-5981.

[3] D. Rosenblum, N. Joshi, W. Tao, J. M. Karp and D. Peer, Progress and challenges towards targeted delivery of cancer therapeutics, *Nature Commun.*, 2018, **9**, 1410.

[4] B. Aslan, B. Ozpolat, A.K. Sood and G. Lopez-Berestein, Nanotechnology in cancer therapy, *J. Drug Target.*, 2013, **21**, 904-913.

[5] H. Maeda, H. Nakamura and J. Fang, The EPR effect for macromolecular drug delivery to solid tumors: Improvement of tumor uptake, lowering of systemic toxicity, and distinct tumor imaging in vivo, *Adv. Drug Deliv. Rev.*, 2013, **65**, 71-79.

[6] M. Morales-Cruz, Y. Delgado, B. Castillo, C. M. Figueroa, A. M. Molina, A. Torres, M. Milián and K. Griebenow, Smart Targeting To Improve Cancer Therapeutics, *Drug Des. Devel. Ther.*, 2019, **13**, 3753-3772.

[7] James D. Byrne, T. Betancourt and L. Brannon-Peppas, Active targeting schemes for nanoparticle systems in cancer therapeutics, *Adv. Drug. Deliv. Rev.*, 2008, **60**, 1615-1626.

[8] J. Yoo, C. Park, G. Yi, D. Lee and H. Koo, Active Targeting Strategies Using Biological Ligands for Nanoparticle Drug Delivery Systems, *Cancers*, 2019, **11**, E640.

[9] R. Bazak, M. Houri, S. El Achy, S. Kamel and T. Refaat, Cancer active targeting by nanoparticles: a comprehensive review of literature, *J. Cancer Res. Clin. Oncol.*, 2015, **141**, 769-784.

[10] M. Vallet-Regí, A. Rámila, R.P. del Real and J. Pérez-Pariente, A New Property of MCM-41: Drug Delivery System, *Chem. Mater.*, 2001, **13**, 308-311.

[11] F. Tang, L. Li and D. Chen, Mesoporous silica nanoparticles: synthesis, biocompatibility and drug delivery, *Adv. Mater.*, 2012, **24**, 1504-1534.

[12] M. Colilla, B. González and M. Vallet-Regí, Mesoporous silica nanoparticles for the design of smart delivery nanodevices, *Biomater. Sci.*, 2013, **1**, 114-134.

[13] R. Castillo, D. Lozano. B. González, M. Manzano, I. Izquierdo and M. Vallet-Regí, Advances in mesoporous silica nanoparticles for targeted stimuli-responsive drug delivery: an update, *Expert Opin. Drug Deliv.*, 2019, **16**, 415-439.

[14] N. Iturrioz-Rodriguez, M.A. Correa-Duarte and M.L. Fanarraga, Controlled drug delivery systems for cancer based on mesoporous silica nanoparticles, *Int. J. Nanomedicine*, 2019, **14**, 3389-3401.

[15] M. Manzano and M. Vallet-Regí, Mesoporous silica nanoparticles for drug delivery, *Adv. Funct. Mater.*, 2020, **30**, E1902634.

[16] V.M. Moreno, E. Álvarez, I. Izquierdo-Barba, A. Baeza, J. Serrano-López and M. Vallet-Regí, Bacteria as nanoparticles carrier for enhancing penetration in a tumoral matrix model, *Adv. Mater. Interfaces*, 2020, 1901942.

[17] X.-F. Zhang, Z.-G. Liu, W. Shen and S. Gurunathan, Silver nanoparticles: synthesis, characterization, properties, applications, and therapeutic approaches, *Int. J. Mol. Sci.*, 2016, **17**, 1534-1567.

[18] D. Kovacs, K. Szoke, N. Igaz, G. Spengler, J. Molnar, T. Toth, D. Madarasz, Z. Razga, Z. Konya, I.M. Boros and M. Kiricsi, Silver nanoparticles modulate ABC transporter activity and enhance chemotherapy in multidrug resistance cancer, *Nanomedicine*, 2016, **12**, 601-610.

[19] L. Wei, J. Lu, H. Xu, A. Patel, Z.-S. Chen and G. Chen, Silver nanoparticles: synthesis, properties, and therapeutic applications, *Drug Discov. Today*, 2015, **20**, 595-601.

[20] C. Ong, J.Z.Z. Lim, J.J. Li, L.-Y.L. Yung and B.-H. Bay, Silver nanoparticles in cancer: therapeutic efficacy and toxicity, *Curr. Med. Chem.*, 2013, **20**, 772-781.

[21] H.J. Johnston, G. Hutchison, F.M. Christensen, S. Peters, S. Hankin and V. Stone, A review of the in vivo and in vitro toxicity of silver and gold nanoparticulates: particle attributes and biological mechanisms responsible for the observed toxicity, *Crit. Rev. Toxicol.*, 2010, **40**, 328-346.

[22] S. Montalvo-Quirós, S. Gómez-Graña, M. Vallet-Regí, R.C. Prados-Rosales, B. González and J.L. Luque-Garcia, Mesoporous silica nanoparticles containing silver as novel antimycobacterial agents against Mycobacterium tuberculosis, *Colloids Surf. B*, 2021, **197**, 111405.

[23] S. Montalvo-Quirós, G. Aragoneses-Cazorla, L. García-Alcalde, M. Vallet-Regí, B. González and J.L. Luque-García, Cancer cell targeting and therapeutic delivery of silver nanoparticles by mesoporous silica nanocarriers: insights into the action mechanisms using quantitative proteomics, *Nanoscale*, 2019, **11**, 4531-4545.

[24] P. Saint-Cricq, J. Wang, A. Sugawara-Narutaki, A. Shimojima and T. Okubo, A new synthesis of well-dispersed, core-shell Ag@SiO_2 mesoporous nanoparticles using amino acids and sugars, *J. Mater. Chem. B*, 2013, **1**, 2451-2454.

[25] C. Ma, Q. Wei, B. Cao, X. Cheng, J. Tian, H. Pu, A. Yusufu and L. Cao, A multifunctional bioactive material that stimulates osteogenesis and promotes the vascularization bone marrow stem cells and their resistance to bacterial infection, *PLoS ONE* 2017, **12**, e0172499.

[26] Y. Wang, X. Ding, Y. Chen, M. Guo, Y. Zhang, X. Guo and H. Gu, Antibiotic-loaded, silver core-embedded mesoporous silica nanovehicles as a synergistic antibacterial agent for the treatment of drug-resistant infections, *Biomaterials*, 2016, **101**, 207-216.

[27] L.T. Zhuravlev, The Surface Chemistry of Amorphous Silica. Zhuravlev Model, *Colloids Surfaces A Physicochem. Eng. Asp.*, 2000, **173**, 1-38.

[28] V.Y.-S. Lin, C.-P. Tsai, H.-Y. Huang, C.-T. Kuo, Y. Hung, D.-M. Huang, Y.-C. Chen and C.-Y. Mou, Well-ordered Mesoporous Silica Nanoparticles as Cell Markers, *Chem. Mater.*, 2005, **17**, 4570-4573.

[29] W.R. Algar, D.E. Prasuhn, M.H. Stewart, T.L. Jennings, J.B. Blanco-Canosa, P.E. Dawson and I.L. Medintz, The controlled display of biomolecules on nanoparticles: a challenge suited to bioorthogonal chemistry, *Bioconjugate Chem.*, 2011, **22**, 825-858.

[30] A. Salvati, A.S. Pitek, M.P. Monopoli, K. Prapainop, F. Baldelli Bombelli, D.R. Hristov, P.M. Kelly, C. Åberg, E. Mahon and K.A. Dawson, Transferrin-functionalized nanoparticles lose their targeting capabilities when a biomolecule corona adsorbs on the surface, *Nature Nanotech.*, 2013, **8**, 137-143.

[31] S. Montalvo-Quirós, M. Vallet-Regí, A. Palacios, J. Anguita, R.C. Prados-Rosales, B. González and J.L. Luque-Garcia, Mesoporous Silica Nanoparticles as a Potential Platform for Vaccine Development against Tuberculosis, *Pharmaceutics* 2020, **12**, 1218.

[32] Á. Martínez, E. Fuentes-Paniagua, A. Baeza, J. Sánchez-Nieves, M. Cicuéndez, R. Gómez, F.J. de la Mata, B. González and M. Vallet-Regí, Mesoporous Silica Nanoparticles Decorated with Carbosilane Dendrons as New Non-viral Oligonucleotide Delivery Carriers, *Chem. Eur. J.*, 2015, **21**, 15651-15666.

[33] Nanomaterials for Food Applications - Micro and Nano Technologies, Elsevier 2019, Pages 313-353. Chapter 11 - Characterization of Nanomaterials: Tools and Challenges. T. Mudalige, H. Qu, D. Van Haute, S.M. Ansar, A. Paredes, T. Ingle.

[34] M. Danaei, M. Dehghankhold, S. Ataei, F. Hasanzadeh Davarani, R. Javanmard, A. Dokhani, S. Khorasani and M.R. Mozafari, Impact of Particle Size and Polydispersity Index on the Clinical Applications of Lipidic Nanocarrier Systems, *Pharmaceutics* 2018, **10**, 57.

[35] J. Tang, Q. Wang, Q. Yu, Y. Qiu, L. Mei, D. Wan, X. Wang, M. Li and Q. He, A stabilized retro-inverso peptide ligando of transferrin receptor for enhanced liposome-based hepatocellular carcinoma-targeted drug delivery, *Acta Biomater.*, 2019, **83**, 379-389.

[36] H. Kawabata, R. Yang, T. Hirama, P.T. Vuong, S. Kawano, A.F. Gombart and H.P. Koeffler, Molecular cloning of transferrin receptor 2. A new member of the transferrin receptor-like family, *J. Biol. Chem.*, 1999, **274**, 20826-20832.

[37] M. Weber, H. Steinle, S. Golombek, L. Hann, C. Schlensak, H. P. Wendel and M. Avci-Adali, Blood-Contacting Biomaterials: In Vitro Evaluation of the Hemocompatibility. *Front. Bioeng. Biotechnol.*, 2018, **6**, 99.

[38] M.F. Matus, C. Vilos, B.A. Cisterna, E. Fuentes and I. Palomo, Nanotechnology and primary hemostasis: Differential effects of nanoparticles on platelet responses, *Vascul. Pharmacol.*, 2018, **101**, 1.

[39] S.K. Austin, Haemostasis, *Medicine*, 2017, **45**, 204.

[40] J. Li, Y. Ying, H. Xie, K. Jin, H. Yan, S. Wang, M. Xu, X. Xu, X. Wang, K. Yang, X. Zheng and L. Xie, Dual regulatory role of CCNA2 in modulating cdk6 and MET-

mediated cell-cycle pathway and EMT progression is blocked by mir-381-3p in bladder cancer, *FASEB J.*, 2018, **33**, 1374-1388.

[41] S. Gao, J. Li, X. Qu, N. Zhu and Y. Ji, Downregulation of Cdk1 and Cyclin B1 expression contributes to oridonin-induced cell cycle arrest at G2/M phase and growth inhibition in SGC-7901 gastric cancer cells, *Asian Pac. J. Cancer Prev.*, 2014, **15**, 6437-6441.

[42] J. Zhou, S. Han, W. Qian, Y. Gu, Z. Li and K. Yang, Metformin induces miR-378 to downregulate the CDK1, leading to suppression of cell proliferation in hepatocellular carcinoma, *Onco. Targets Ther.*, 2018, **11**, 4451-4459.

[43] M.R. Theoret, C.J. Cohen, A.V. Nahvi, L.T. Ngo, K.B. Suri, D.J. Powell Jr., M.E. Dudley, R.A. Morgan and S-A. Rosenberg, Relationship of p53 overexpression on cancers and recognition by anti-p53 T cell receptor-transduced T cells, *Hum. Gene Ther.*, 2008, **19**, 1219-1231.

[44] Y. Cahi, L. Xiaoyu and W. Haiyan, Correlation between expression levels of PTEN and p53 genes and the clinical features of HBsAg-positive liver cancer, *J. BUON*, 2017, **22**, 942-946.

[45] P.B.S. Lai, T.-Y. Chi and G. G. Chen, Different levels of p53 induced either apoptosis or cell cycle arrest in a doxycycline-regulated hepatocellular carcinoma cell line *in vitro*, *Apoptosis*, 2007, **12**, 387-393.

[46] N.K. Dhillon and M. Mudryj, Cyclin E overexpression enhances cytokine-mediated apoptosis in MCF7 breast cancer cells, *Genes Immun.*, 2003, **4**, 336-342.

[47] O. Nehls, T. Okech, C.J. Hsieh, T Enzinger, M. Sarbia, F. Borchard, H.H. Gruenagel, V. Gaco, H.G. Hass, H.T. Arkenau, J.T. Hartmann, R. Porschen, M. Gregor and B. Klump, Studies on p53, BAX and Bcl-2 protein expression and microsatellite instability in stage III (UICC) colon cancer treated by adjuvant chemotherapy: major prognostic impact of proapoptotic BAX, *Br. J. Cancer*, 2007, **96**, 1409-1418.

[48] F. Gonzalvez and A. Ashkenazi, New insights into apoptosis signaling by Apo2L/TRAIL, *Oncogene*, 2010, **29**, 4752-4762.

[49] H-B. Wang, T. Li, D-Z. Ma, Y-X. Ji and H. Zhi, Overexpression of FADD and Caspase-8 inhibits proliferation and promotes apoptosis of human glioblastoma cells, *Biomed. Pharmacother.*, 2017, **93**, 1-7.

[50] A. Penna, N. Khadra, S. Tauzin, P. Vacher and P. Legembre, The CD95 signaling pathway, *Commun. Integr. Biol.*, 2012, **5**, 190-192.

[51] P-F. Liu, Y-C. Hu, B-H. Kang, Y-K. Tseng, P-C. Wu, C-C. Liang, Y-Y. Hou, T-Y. Fu, H-H. Liou, I-C. Hsieh, L-P. Ger and C-W. Shu, Expression levels of cleaved caspase-3 and caspase-3 in tumorigenesis and prognosis of oral tongue squamous cell carcinoma, *PLoS ONE*, 2017, **12**, e0180620.

[52] K. Friedrich, T. Wieder, C. Von Haefen, S. Radetzki, R. Jänicke, K. Schulze-Osthoff, B. Dörken and P. T. Daniel, Overexpression of caspase-3 restores sensitivity for drug-induced

apoptosis in breast cancer cell lines with acquired drug resistance, *Oncogene*, 2001, **20**, 2749-2760.

[53] S.B. McMahon, MYC and the control of apoptosis, *Cold Spring Harb. Perspect. Med.*, 2014, **4**, a014407.

[54] B. Hoffman and D.A. Liebermann, Apoptotic signaling by c-MYC, *Oncogene*, 2008, **27**, 6462-6472.

[55] H. Huang, K.M. Regan, Z. Lou, J. Chen and D.J. Tindall, CDK2-Dependent phosphorylation of FOXO1 as an apoptotic response to DNA damage, *Science*, 2006, **314**, 294-297.

[56] M.E. Lane, B. Yu, A. Ric, K. E. Lipson, C. Liang, L. Sun, C. Tang, G. McMahon, R. G. Pestell and S. Wadler, A novel cdk2-selective inhibitor, SU9516, induces apoptosis in colon carcinoma cells, *Cancer Res.*, 2001, **15**, 6170-6177.

[57] Y. Matthess, M. Raab, M. Sanhaji, I. N. Lavrik and K. Strebhardt, Cdk1/cyclin B1 controls Fas-mediated apoptosis by regulating caspase-8 activity, *Mol. Cell. Biol.*, 2010, **30**, 5726-5740.

[58] A. Karimian, Y. Ahmadi and B. Yousefi, Multiple functions of p21 in cell cycle, apoptosis and transcriptional regulation after DNA damage, *DNA Repair*, 2016, **42**, 63-71.

[59] J.Y. Lee, H.S. Kim, J.Y. Kim and J. Sohn, Nuclear translocation of p21WAF1/CIP1 protein prior to its cytosolic degradation by UV enhances DNA repair and survival, *Biochem. Biophys. Res. Commun.*, 2009, **390**, 1361-1366.

[60] Supriatno, K. Harada, M.O. Hoque, T. Bando, H. Yoshida and M. Sato, Overexpression of p27Kip1 induces growth arrest and apoptosis in an oral cancer cell line, *Oral Oncol.*, 2002, **38**, 730-736.

[61] D. Merino, S.W. Lok, J.E. Visvader and G.J. Lindeman, Targeting BCL-2 to enhance vulnerability to therapy in estrogen receptor-positive breast cancer, *Oncogene*, 2016, **35**, 1877-1887.

[62] L. Jiang, M. Luo, D. Liu, B. Chen, W. Zhang, L. Mai, J. Zeng, N. Huang, Y. Huang, X. Mo and W. Li, BAD overexpression inhibits cell growth and induces apoptosis via mitochondrial-dependent pathway in non-small cell lung cancer, *Cancer Cell Int.*, 2013, **13**, 53-63.

[63] A.J. Smith, Y. Karpova, R.D’Agostino, M. Willingham and G. Kulik, Expression of the Bcl-2 protein BAD promotes prostate cancer growth, *PLoS ONE*, 2009, **4**, e6224.

[64] J.C. Goldstein, N.J. Waterhouse, P Juin, G. I. Evan and D.R. Green, The coordinate release of cytochrome c during apoptosis is rapid, complete and kinetically invariant, *Nat. Cell Biol.*, 2000, **2**, 156-162.

[65] G. Martinez-Ruiz, V. Maldonado, G. Ceballos-Cancino, J.P. Reyes-Grajeda, and J. Melendez-Zajgla, Role of Smac/DIABLO in cancer progression, *J. Exp. Clin. Cancer Res.*, 2008, **27**, 48-54.

[66] L. van de Walle, M. Lamkanfi and P. Vandenabeele, The mitocondrial serine protease HtrA2/Omi: an overview, *Cell Death Differ.*, 2008, **15**, 453-460.

[67] J-P. Piret, E. Minet, J-P. Cosse, N. Ninane, C. Debacq, M. Raes and C. Michiels, Hypoxia-inducible factor-1-dependent overexpression of myeloid cell factor-1 protect hypoxic cells against tert-butyl hydroperoxide-induced apoptosis, *J. Biol. Chem.*, **2005**, *280*, 9336-9344.

[68] A.E. Greijer and E. van der Wall, The role of hypoxia inducible factor 1 (HIF-1) in hypoxia induced apoptosis, *J. Clin. Pathol.*, 2004, **57**, 1009-1014.

[69] X. Chen, N. Duan, C. Zhang and W. Zhang, Survivin and tumorigenesis: molecular mechanisms and therapeutic strategies, *J. Cancer*, 2016, **7**, 314-323.

[70] I. Esposito, J. Kleef, I. Abiatari, X. Shi, N. Giese, F. Bergmann, W. Roth, H. Friess and P. Schirmacher, Overexpression of cellular inhibition of apoptosis protein 2 is an early event in the progression of pancreatic cancer, *J. Clin. Pathol.*, 2007, **60**, 885-895.

[71] C. Van Themsche, P. Chaudhry, V. Leblanc, S. Parent and E. Asselin, XIAP gene expression and function is regulated by autocrine and paracrine TGF-beta signaling, *Mol. Cancer*, 2010, **9**, 216-227.

[72] F. Li, L. Zhang, F. Feng, K. Zheng, Y. Li, T. Wang and G. Ren, Livin participates in resistance to trastuzumab therapy for breast cancer through ERK1/2 and AKT pathways and promotes EMT-like phenotype, *RSC Adv.*, 2018, **8**, 28588-28601.

[73] B. Herrera, M. Fernández, M. Benito and I. Fabregat, cIAP-1, but not XIAP, is cleaved by caspases during the apoptosis induced by TGF-b in fetal rat hepatocytes, *FEBS Lett.*, 2002, **520**, 93-96.

[74] A. Vidyasagar, N.A. Wilson and A. Djamali, Heat shock protein 27 (HSP27): biomarker of disease and therapeutic target, *Fibrogenesis Tissue Repair*, 2012, **5**, 7-13.

[75] U. Sarangi, M.K. Singh, K.V.V. Abhijnya, L.P.A. Reddy, B.S. Prasad, V.V. Pitke, K. Paithankar and A.S. Sreedhar, Hsp60 chaperonin acts as barrier to pharmacologically induced oxidative stress mediated apoptosis in tumor cells with differential stress response, *Drug Target Insights*, 2013, **7**, 35-51.

[76] M.E. Murphy, The HSP70 family and cancer, *Carcinogenesis*, 2013, **34**, 1181-1188.

[77] P. Banerjee, A. Basu, B. Wegiel, L.E. Otterbein, K. Mizumura, M. Gasser, A.M. Waada-Gasser, A. M. Choi and S. Pal, Hemeoxygenase-1 promotes survival of renal cancer cells through modulation of apoptosis- and autophagy-regulating molecules, *J. Biol. Chem.*, 2012, **287**, 32113-32123.

[78] J. Muñoz-Sánchez and M.E. Chánez-Cárdenas, A review on hemeoxygenase-2: focus on celular protection and oxygen response, *Oxid. Med. Cell. Longev.*, 2014, **2014**, 604981.

[79] X. Wang, L. Zou, T. Lu, S. Bao, K.E. Hurov, W.N. Hittleman, S.J. Elledge and L. Li, Rad17 phosphorylation is required for claspin recruitment and Chk1 activation in response to replication stress, *Mol. Cell*, 2004, **23**, 331-341.

[80] S. Post, Y.-C. Weng, K. Cimprich, L.B. Chen, Y. Xu and E.Y-.H.P. Lee, Phosphorylation of serines 635 and 645 of human Rad17 is cell cycle regulated and is required for G1/S checkpoint activation in response to DNA damage, *Proc. Natl. Acad. Sci.*, 2001, **98**, 13102-13107.

[81] N. Mailand, S. Bekker-Jensen, J. Bartek and J. Lukas, Destruction of claspin by SCFbTrCP restrains Chk1 activation and facilitates recovery from genotoxic stress, *Mol. Cell*, 2006, **23**, 307-318.

[82] F. Ito, C. Yoshimoto, Y. Yamada, T. Sudo and H. Kobayashi, The HNF-1b-USP28-Claspin pathway upregulates DNA damage-induced Chk1 activation in ovarian clear cell carcinoma, *Oncotarget*, 2018, **9**, 17512-17522.

[83] L. Flanagan, L. Whyte, N. Chtterjee and M. Tenniswood, Effects of clusterin over-expression on metastatic progression and therapy in breast cancer, *BMC Cancer*, 2010, **10**, 107-121.

[84] M. Scaltriti, S. Bettuzzi, R.M. Sharrard, A. Caporali, A.E. Caccamo and B.J. Maitland, Clusterin overexpression in both malignant and nonmalignant prostate epithelial cells induces cell cycle arrest and apoptosis, *Br. J. Cancer*, 2004, **91**, 1842-1850.

Table of Contents entry

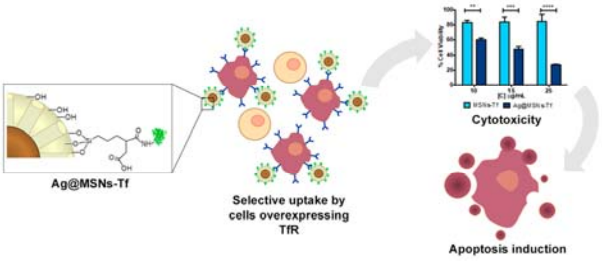

Synthesis, characterization and evaluation of transferrin-decorated mesoporous silica-coated silver nanoparticles as a novel hemocompatible core@shell nanosystem for selective targeting and apoptosis induction in cancer cells

Table 1. Organic content and elemental composition from thermogravimetric and chemical analysis of Ag@MSNs and functionalized Ag@MSNs materials.

Material	Org. Content (wt %)	%C	%N	%S
Ag@MSNs	5.33 [a]	2.13	0.12	0.00
Ag@MSNs-COOH$_{ext}$	6.95 [a,b]	6.53	0.33	0.01
Ag@MSNs-Tf	15.49 [a,b]	11.01	2.08	0.13

[a] Organic content (wt%) is determined from the TGA weight losses, excluding the weight loss due to the desorption of water (up to 125 °C) and [b] further corrected by the weight loss of the remaining alkoxysilanes after the sol-gel reaction (surfactant extracted unmodified Ag@MSNs).

Table 2. ζ-Potential values and hydrodynamic particle size in water medium of Ag@MSNs and functionalized Ag@MSNs materials.

Material	ζ-Potential [a] (mV)	Hydrodynamic size [a,b] (nm)
Ag@MSNs	−14 ± 3	68 ± 6
Ag@MSNs-COOH$_{ext}$	−26 ± 6	59 ± 5
Ag@MSNs-Tf	−20 ± 6	79 ± 8

[a] Samples were measured in quintuplicate (n = 5). [b] Maximum of the size distribution measured by dynamic light scattering.

Figure Legends

Fig. 1. Synthetic procedure for (A) Ag@MSNs and (B) Ag@MSNs-Tf.

Fig. 2. TEM micrographs of Ag@MSNs (A and B), Ag@MSNs-COOH$_{ext}$ (C) and Ag@MSNs-Tf (D) materials at different magnifications. EDS analysis of Ag@MSNs is shown as an inset in A.

Fig. 3. Fourier transformed infrared (FTIR) spectra of Ag@MSNs, Ag@MSNs-COOH and Ag@MSNs-Tf nanosystems. # Bands due to physisorbed water.

Fig. 4. Differential cellular internalization evaluated on HepG2 and MC3T3-E1 cells exposed to 50 µg/mL of Ag@MSNs or Ag@MSNs-Tf for 24 h. Data were analyzed by ANOVA followed by Bonferroni's multiple-comparison test. Statistical significance: **** $p<0.0001$.

Fig. 5. (A) Cell viability of HepG2 cells exposed to different concentrations (10, 15 and 25 µg/mL) of MSNs-Tf or Ag@MSNs-Tf for 72 h. (B) Percentage of HepG2 dead cells after treatment to different concentrations of MSNs-Tf and Ag@MSNs-Tf (10 and 25 µg/mL) for 72 h. Data were analyzed by ANOVA followed by Bonferroni's multiple-comparison test. Statistical significance: ** $p< 0.01$. *** $p< 0.001$. **** $p<0.0001$.

Fig. 6. Circulating monocytes activation (upper row): (A) representative gating strategy for monocytes analysis (blue) by flow cytometry; (B) bar graphs represent fold increase of Mean Fluorescent Intensity (MFI) for CD16 (left panel) and CD11B (right panel) surface markers on monocytes after nanoparticles insult. To normalize the data, a negative control without nanoparticles was used to calculate the ratio. Values represent mean ± SD of a minimum of 3 healthy donor. Platelet activation (bottom row): (C) representative real time curves of citrate platelet rich plasma (PRP) after nanoparticles insult or soluble agonists such as epinephrine (black curve) or thrombin-like peptides (red curve); (D) graph represents the percentage of platelet sedimentation after being in contact with different nanoparticles at scaled doses.

Fig. 7. (A) Cell cycle pattern analyzed by flow cytometry and (B) mRNA levels of genes related to cell cycle regulation of HepG2 cells treated with 10 µg/mL of Ag@MSNs-Tf for 72 h. Untreated HepG2 cells were used as control. Data were analyzed by ANOVA followed by Bonferroni's multiple-comparison test. Statistical significance: "ns" non-significant; *** $p<0.001$; **** $p<0.0001$.

Fig. 8. Expression levels of (A) cell cycle-related proteins, (B) pro-apoptotic proteins and (C) defense proteins of HepG2 cells treated with 10 µg/mL of Ag@MSNs-Tf for 72 h. Untreated HepG2 cells were used as control. Data were analyzed by ANOVA followed by Bonferroni's multiple-comparison test. Statistical significance: "ns" non-significant; * $p<0.05$; **$p<0.01$; *** $p<0.001$, **** $p<0.0001$.

Fig. 9 Illustration of (A) cell cycle-related apoptosis, (B) pro-apoptotic and (C) cellular defense mechanisms involved in the action exerted by Ag@MSNs-Tf nanosystems on HepG2 cells.

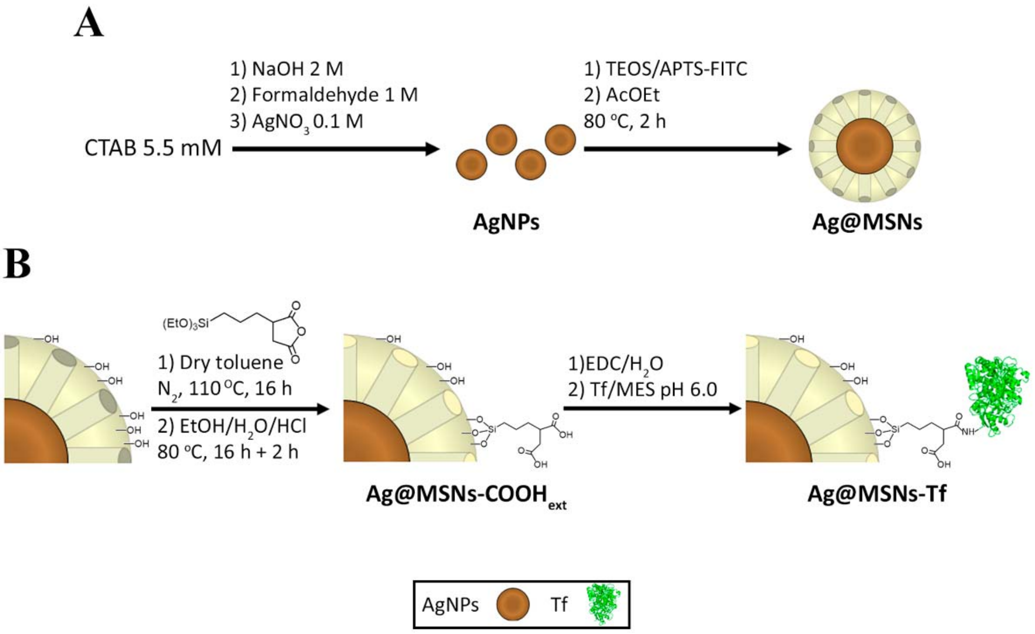

Fig. 1. Synthetic procedure for (A) Ag@MSNs and (B) Ag@MSNs-Tf.

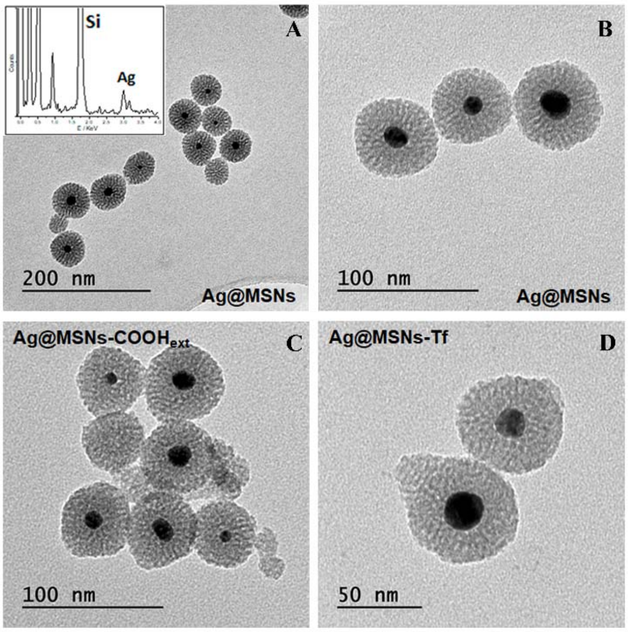

Fig. 2. TEM micrographs of Ag@MSNs (A and B), Ag@MSNs-COOH$_{ext}$ (C) and Ag@MSNs-Tf (D) materials at different magnifications. EDS analysis of Ag@MSNs is shown as an inset in A.

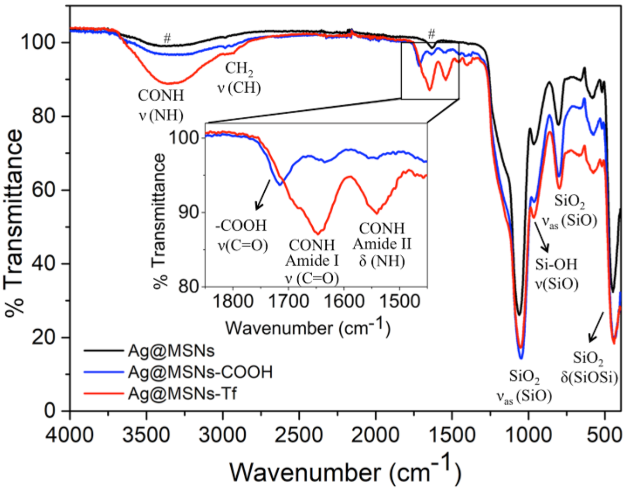

Fig. 3. Fourier transformed infrared (FTIR) spectra of Ag@MSNs, Ag@MSNs-COOH and Ag@MSNs-Tf nanosystems. # Bands due to physisorbed water.

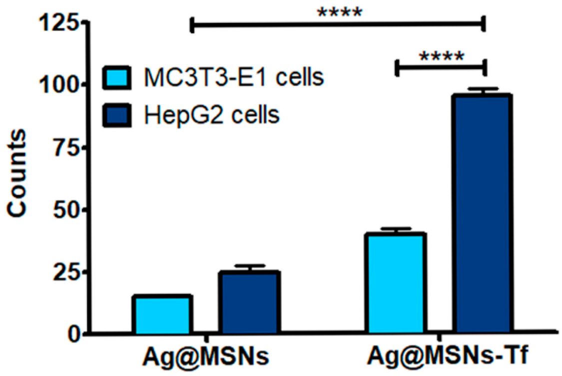

Fig. 4. Differential cellular internalization evaluated on HepG2 and MC3T3-E1 cells exposed to 50 µg/mL of Ag@MSNs or Ag@MSNs-Tf for 24 h. Data were analyzed by ANOVA followed by Bonferroni's multiple-comparison test. Statistical significance: **** $p<0.0001$.

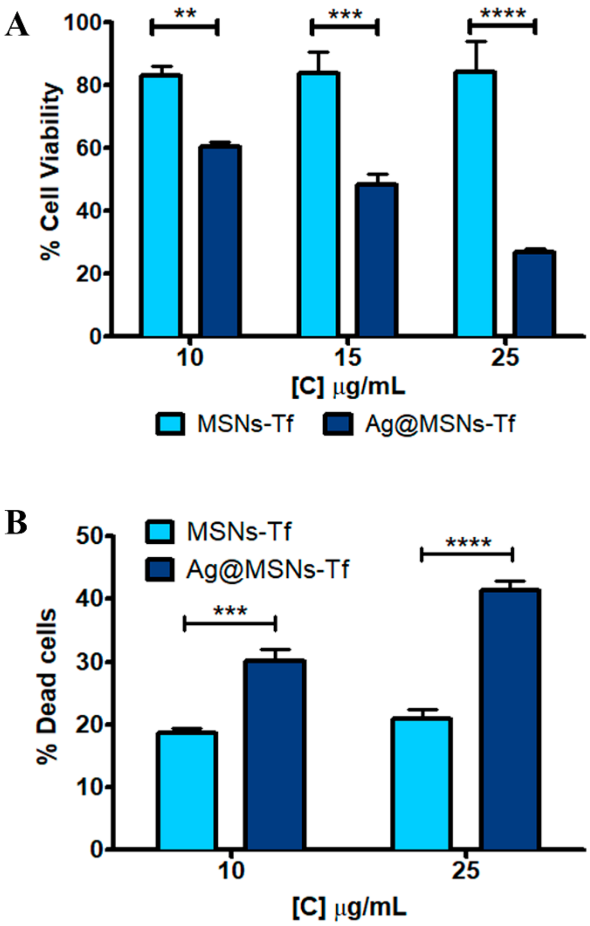

Fig. 5. (A) Cell viability of HepG2 cells exposed to different concentrations (10, 15 and 25 μg/mL) of MSNs-Tf or Ag@MSNs-Tf for 72 h. (B) Percentage of HepG2 dead cells after treatment to different concentrations of MSNs-Tf and Ag@MSNs-Tf (10 and 25 μg/mL) for 72 h. Data were analyzed by ANOVA followed by Bonferroni's multiple-comparison test. Statistical significance: ** $p < 0.01$. *** $p < 0.001$. **** $p < 0.0001$.

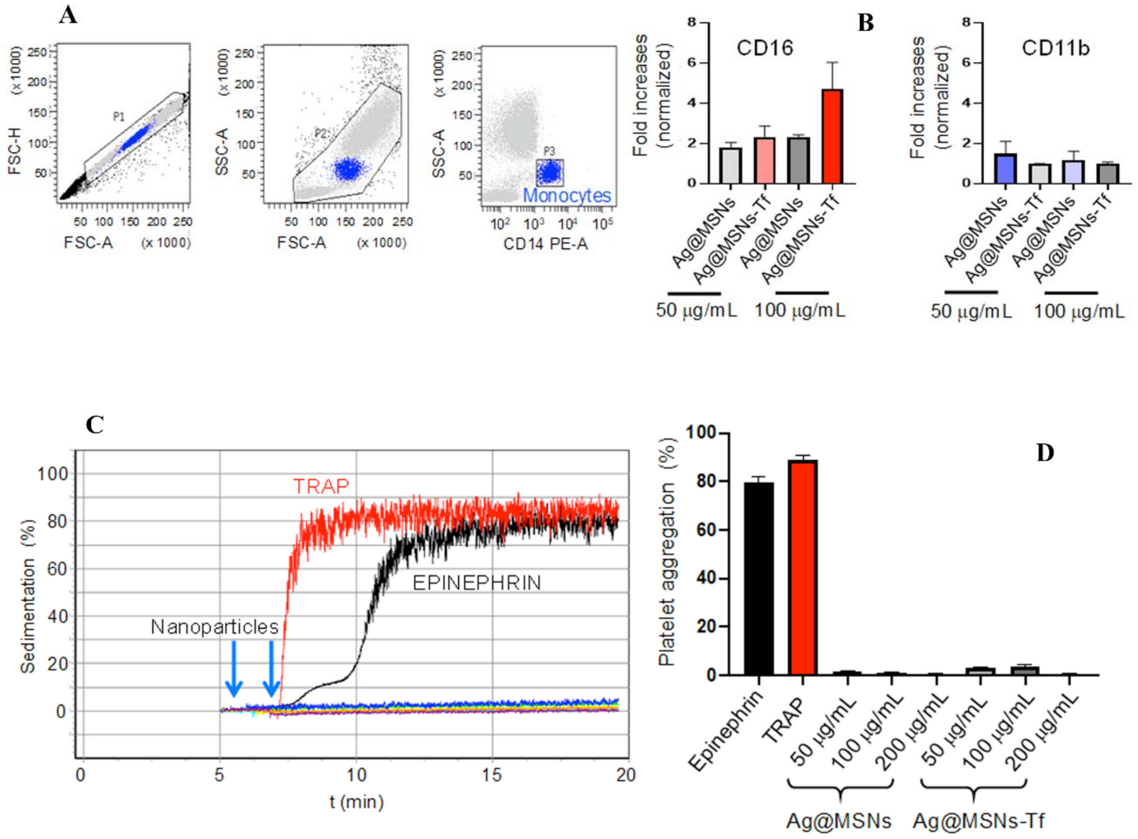

Fig. 6. Circulating monocytes activation (upper row): (A) representative gating strategy for monocytes analysis (blue) by flow cytometry; (B) bar graphs represent fold increase of Mean Fluorescent Intensity (MFI) for CD16 (left panel) and CD11B (right panel) surface markers on monocytes after nanoparticles insult. To normalize the data, a negative control without nanoparticles was used to calculate the ratio. Values represent mean ± SD of a minimum of 3 healthy donor. Platelet activation (bottom row): (C) representative real time curves of citrate platelet rich plasma (PRP) after nanoparticles insult or soluble agonists such as epinephrine (black curve) or thrombin-like peptides (red curve); (D) graph represents the percentage of platelet sedimentation after being in contact with different nanoparticles at scaled doses.

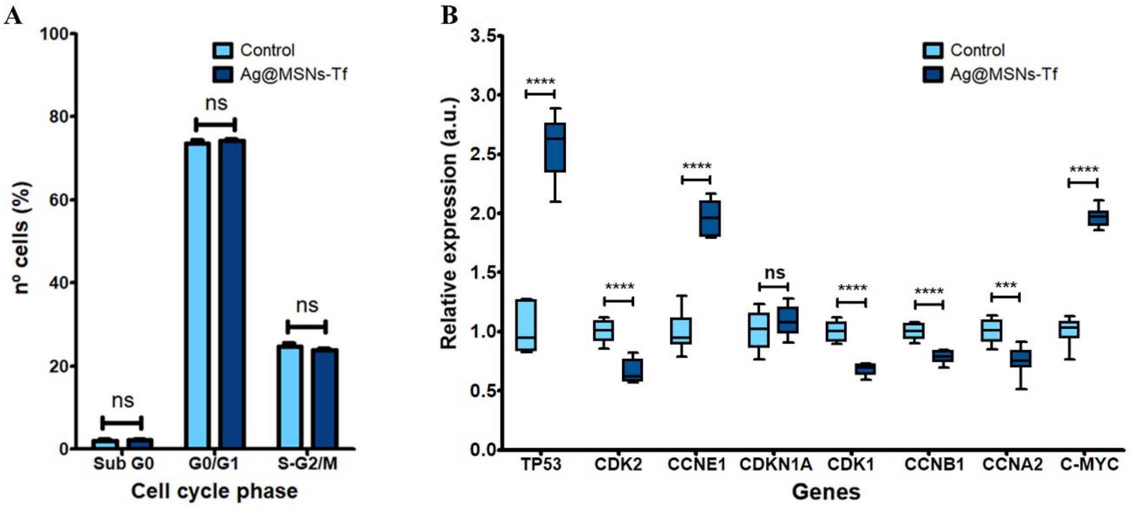

Fig. 7. (A) Cell cycle pattern analyzed by flow cytometry and (B) mRNA levels of genes related to cell cycle regulation of HepG2 cells treated with 10 µg/mL of Ag@MSNs-Tf for 72 h. Untreated HepG2 cells were used as control. Data were analyzed by ANOVA followed by Bonferroni's multiple-comparison test. Statistical significance: "ns" non-significant; *** p<0.001; **** p<0.0001.

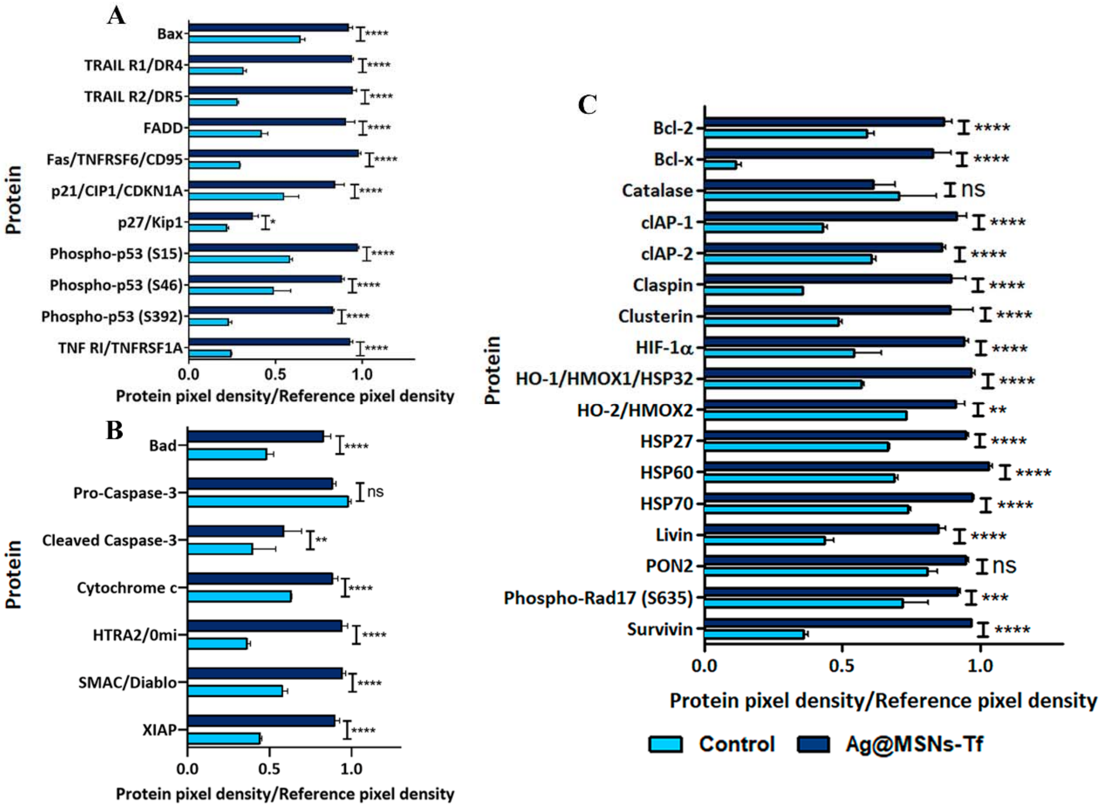

Fig. 8. Expression levels of (A) cell cycle-related proteins, (B) pro-apoptotic proteins and (C) defense proteins of HepG2 cells treated with 10 µg/mL of Ag@MSNs-Tf for 72 h. Untreated HepG2 cells were used as control. Data were analyzed by ANOVA followed by Bonferroni's multiple-comparison test. Statistical significance: "ns" non-significant; * p<0.05; **p<0.01; *** p<0.001, **** p<0.0001.

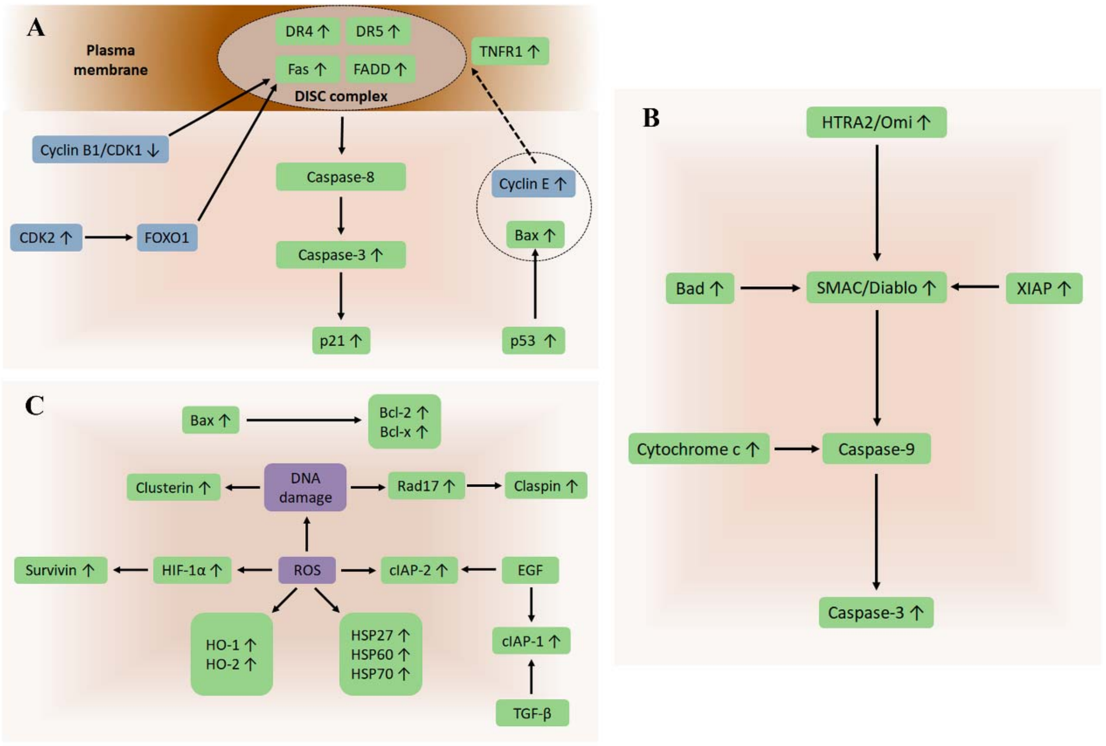

Fig. 9 Illustration of (A) cell cycle-related apoptosis, (B) pro-apoptotic and (C) cellular defense mechanisms involved in the action exerted by Ag@MSNs-Tf nanosystems on HepG2 cells.